In Proceedings of ICRA 2001
IEEE Conference on Robotics and Automation
pages 3901-8, May 2001, Seoul, Korea

Towards Flapping Wing Control for a Micromechanical Flying Insect *

J. Yan R.J. Wood S. Avadhanula M. Sitti R.S. Fearing

Dept of EECS, University of California, Berkeley, CA 94720
{*joeyan, rjwood, srinath, sitti, ronf*}*@robotics.eecs.berkeley.edu*

Abstract

A 2 DOF resonant thorax structure has been designed and fabricated for the MFI project. Miniature piezoelectric PZN-PT unimorph actuators were fabricated and used to drive a four-bar transmission mechanism. The current thorax design utilizes two actuated four-bars and a spherical joint to drive a rigid wing. Rotationally compliant flexure joints have been tested with lifetimes over 10^6 *cycles. Wing spars were instrumented with strain gauges for force measurement and closed-loop wing control.*

1 Introduction

Micro aerial vehicles (MAVs) have attained a great deal of attention in the past decade due to favorable feasibility studies. Commercial and military applications for such robotic devices have been identified including operations in hazardous environments (*e.g.,* search-and-rescue within collapsed buildings, nuclear plant exploration during a radiation leak, *etc.*) and defense-related missions (*e.g.,* reconnaissance and surveillance).

Although several groups have worked on MAVs based on fixed or rotary wings (*e.g.* [10]), flapping flight provides superior maneuverability which would be beneficial in obstacle avoidance and necessary for navigation in small spaces, as demonstrated by biological flying insects. It has long been known that insect flight cannot be explained by steady state aerodynamics and only in recent years has there been elucidation of the unsteady aerodynamic mechanisms which account for the large lift forces generated. Francis and Cohen appear to have been the first to study impulsive wing translational motions which give rise to the phenomenon known as *delayed stall* [8]; this effect has recently been quantified using a scaled model of a hawkmoth by Ellington *et al* [5]. Dickinson *et al* observed that this phenomenon was inadequate in accounting for the total lift and, using a dynamically-scaled model of a fruitfly, established two additional important lift mechanisms: *rotational circulation* and *wake capture* [4]. The success of flapping MAVs depends on exploitation of all three mechanisms.

Shimoyama pioneered work in micro-robotic flight ([13], [9]) while milli-robotic flapping flight has been pursued by several other groups ([3], [11]). Early work on the UC Berkeley micromechanical flying insect (MFI) was described by Fearing *et al* in [7] while some of the basic thorax fabrication techniques were presented by Shimada *et al* in [12].

This paper describes aspects of the MFI in the areas of mechanical design and fabrication, actuation and sensing, and wing control.

2 Kinematics and Fabrication

Figure 1 illustrates the proposed components of the MFI along with a photo of a mock-up fabricated to scale but without actuation. The design specifications, as outlined in [7], are summarized as follows: $100mg$ mass, $25mm$ wingspan, $150Hz$ wingbeat frequency, $8mW$ of mechanical power delivered to both wings, and each wing must independently have 140^o flapping range and 90^o rotation range (these last two requirements, coupled with the bandwidth, are necessary to exploit the unsteady aerodynamic mechanisms described in section 1).

2.1 Four-bar Kinematics

The basic mechanical transmission element in this design is the four-bar mechanism. Figure 2 illustrates an early cable-driven design in which lateral actuation of the piezoelectric unimorph tip P_2 in one direction causes tension on one side of cable C_1C_2, resulting in a net rotation of the wing spar. The structure was fabricated and driven by the final-sized single-crystal PZN-PT unimorph actuator at a frequency of $44Hz$ for a stroke angle of roughly 60^o. For the link parameters chosen, a simple kinematic analysis shows that piezo

*This work was funded by ONR MURI N00014-98-1-0671 and DARPA.

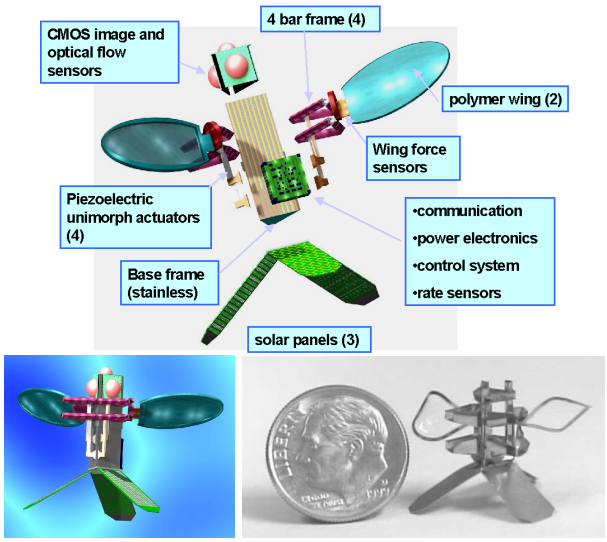

Figure 1: (a) Pre-assembled view showing modular components; (b) Conceptual drawing of MFI; (c) Structural mock-up at final scale.

motion as small as $\pm 0.25mm$ should provide as much as $\pm 70^o$ of spar motion. This motion range was not achieved primarily due to alignment problems during construction and compliance in the flexures and cable.

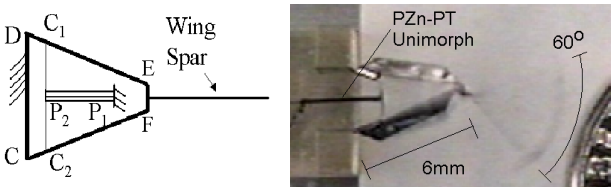

Figure 2: (a) Cable-driven four-bar; (b) Structure driven over 60^o at $44Hz$ by PZN-PT unimorph

This early experiment demonstrates that the single-crystal PZN-PT unimorph actuators, which are intended for the final product, can be fabricated at the desired scale (in the photo, the unimorph is $5mm \times 1mm \times 0.2mm$, with a $150\mu m$ thick PZN-PT plate bonded to a $50\mu m$ thick steel plate) and appear to provide the necessary actuation requirements. The PZN-PT in the photo was driven at only a third of the electric field which it can sustain so much larger displacements are achievable and the resonant frequency can be increased significantly by reducing the structural compliance. Current structures are driven by PZT unimorph actuators which are larger but much cheaper and easier to fabricate. More details about the piezoelectric unimorph fabrication and testing is described by Sitti *et al* in [14].

Figure 3(a) shows the current four-bar dimensions used. The actuation from the piezo unimorph goes through a 2-step amplification (this design, in which link CF is fixed and link CD is driven, provides greater motion amplification than the design of Figure 2(a) in which link CD is fixed and links CF and DE are alternately driven). An initial slider-crank mechanism, converts approximately linear motion at A into rotary motion for link BC. The four-bar CDEF converts this small angular motion at the input link CD to a large rotation for the spar. The relation between the driving input δ and the spar output θ is shown in Figure 3(b). The four-bar structure will be driven at high amplitudes where nonlinearity needs to be considered.

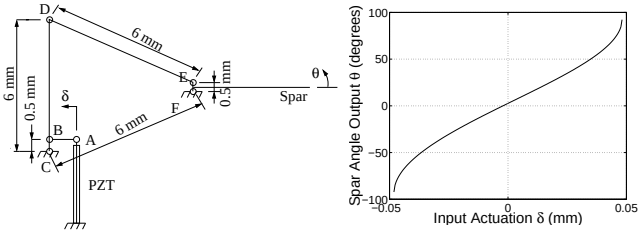

Figure 3: (a) Four-bar dimensions; (b) Ideal I/O characteristics.

Figure 3(b) illustrates that an input actuation of $0.1mm$ is sufficient to get spar output motion of over 180^o, for the ideal four-bar with pinjoints connecting adjacent links. In practice, roughly $0.5mm$ was required for this amount of output due to the joints being flexures, poor adhesion between the flexures and the links, *etc.* Photos of the four-bar near both singularities are shown in Figure 4. Flexures which can accommodate the large angle changes experienced at joints E and F are discussed in section 2.3.

2.2 2 DOF Wing Spar Kinematics

Early work with the "fan-fold" wing described in [7] suggested large losses in the lift force due to billowing out of the wing. This section describes the mechanism by which a rigid wing can be actuated with 2 DOF.

The required flapping and rotation motions of a single wing can be achieved from the wing differential design of Figure 5. It consists of two wing spars, OA and BC, each driven by two independently actuated four-bars. The actuated angles are α_1 and α_2. The *leading spar* BC is restricted to move parallel to the E_1E_2 plane while the *lagging spar* OA possesses a passive DOF, permitting movement out of plane E_1E_2. The wing is coplanar to OAC. Simple flapping motion is achieved by setting $\alpha_1 = \alpha_2$ (*i.e.* spars are actuated in phase). When $\alpha_1 \neq \alpha_2$, (*i.e.* the two spars

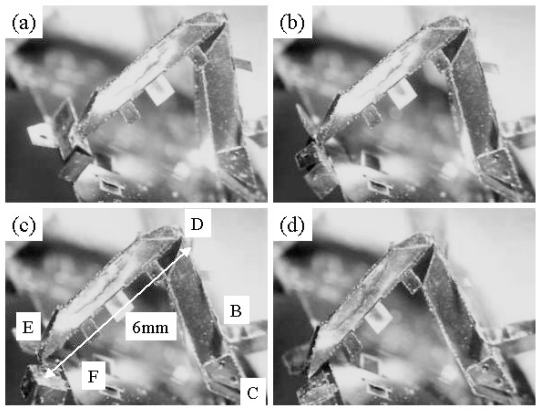

Figure 4: Four-bar at various stages of motion range (observe motion of link EF to which the spar is attached). Labels in (c) correspond to labels of Figure 3a.

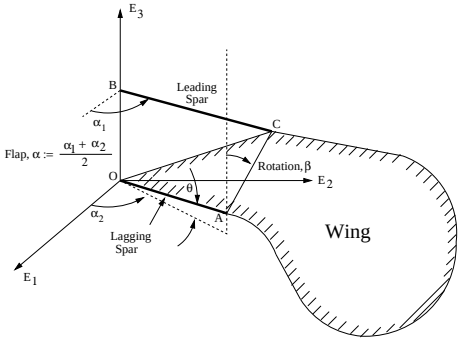

Figure 5: Kinematics of wing differential

are driven out of phase as shown in the figure) the lagging spar moves up through an angle θ so that the distance AC is maintained constant. The flapping angle α can be calculated as the mean of the actuated angles ($\alpha = \frac{\alpha_1+\alpha_2}{2}$). For fixed spar lengths and a fixed spar separation distance, the rotation is only a function of the difference in the actuated angles (*i.e.,* $\beta = \beta(\alpha_2 - \alpha_1)$). For spars $4mm$ long and separated by $1mm$, a phase difference of only $+12^o$ is sufficient to cause a rotation of $\beta = +45^o$.

In this design, a large ratio of $\frac{OA}{AC}$ provides a large variation in the attack angle for a small phase difference ($\alpha_1 - \alpha_2$) and the angle θ. This enables use of a flexure between OA and AC. A spherical joint employed at C allows for all the motion required between AC and BC. The spherical joint consists of a series of 3 flexural joints between BC and AC as shown in Figure 6.

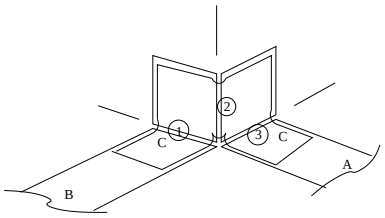

Figure 6: Spherical joint design

An assembled wing differential, attached to two four-bars, is shown in Figure 7. Experimental results with this mechanism with a wing attached are discussed in section 3.

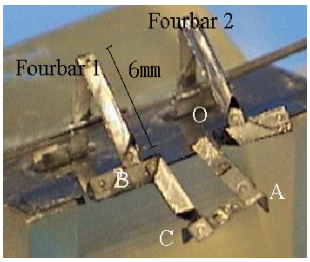

Figure 7: Photo of wing differential mounted on 2 fourbars (labels correspond to those of Figure 5).

2.3 Flexure Design and Fabrication

The target operating time for the MFI is roughly 10 minutes, which at $150Hz$, is equivalent to 10^5 cycles. The flexures are likely failure points and must be designed to endure this level of fatigue stress.

The flexures permit the desired rotational compliance between two links but also unwanted translational compliance. By making the flexure length, l, smaller, they can better simulate ideal pin joints. Unfortunately, shorter flexures also result in higher induced stresses for a given joint angle, restricting the minimum flexure lengths.

Preliminary fatigue tests demonstrated that steel flexures would not survive the required level of cyclic stresses (see Figure 8a) so they were replaced with polyester flexures. The following analysis explains their superior performance.

For a beam section of thickness t, bent into a circular arc of radius ρ and made of a material with Young's modulus E, Poisson ratio ν and yield stress S_Y, the maximum stress σ_{max} occurs at the surface:

$$\sigma_{max} = \frac{Et}{2(1-\nu^2)\rho} \quad (1)$$

Assuming the von Mises yield criterion in which plastic deformation occurs when $\sigma_{max} = \frac{S_Y}{\sqrt{1-\nu+\nu^2}}$, the

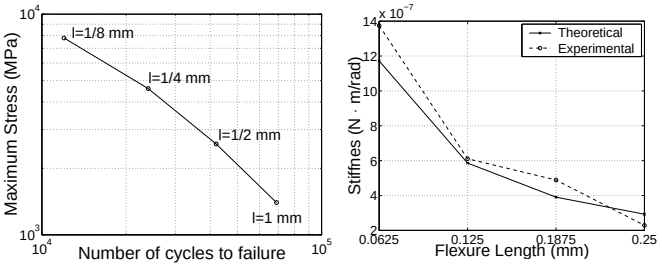

Figure 8: (a) Fatigue test results using steel flexures of lengths from $\frac{1}{8}mm$ to $1mm$; (b) Flexure rotational stiffness vs. length for $6.25\mu m$ polyester.

corresponding radius ρ_Y at which yielding occurs is:

$$\rho_Y = \frac{Et\sqrt{1-\nu+\nu^2}}{2(1-\nu^2)S_Y} = \frac{t\sqrt{1-\nu+\nu^2}}{2(1-\nu^2)\epsilon_Y} \qquad (2)$$

For nonlinear materials, the latter part of the equation using the yield strain ϵ_Y is more appropriate.

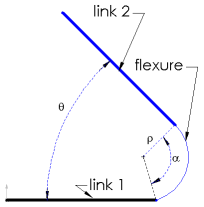

Figure 9: Flexure stress analysis

Consider Figure 9 in which the flexure connects two links at an angle θ. The flexure angle is $\alpha = \pi - \theta = l/\rho$. Given a minimum angle θ, the minimum flexure length is:

$$l_{min} = \rho_Y \alpha = \frac{t(\pi-\theta)\sqrt{1-\nu+\nu^2}}{2(1-\nu^2)\epsilon_Y} \qquad (3)$$

According to this equation, an AISI 302 stainless steel flexure having $\epsilon_Y = 0.14\%$, $t = 12.5\mu m$ and experiencing an angle of $\theta = 40^o$, would need to be at least $l_{min} = 10.3mm$ long to avoid yielding. Replacing this with a polyester flexure having $\epsilon_Y = 4\%$, the flexure would only need to be $l_{min} = 0.38mm$ long. This is a conservative estimate because some level of yielding is permitted. In fact, polyester flexures $0.125mm$ in length were tested over 10^6 cycles without failure. From this study, it is clear that polymers or other materials which have a high yield strain are required for these flexures.

Experiments and analysis of $12.5\mu m$ thick polyester flexures demonstrate that they are too stiff relative to the overall structural stiffness. Recently, $6.25\mu m$ thick polyester has been employed, reducing the flexure stiffness by a factor of 8 which is acceptable. Figure 8b shows how flexure rotational stiffness varies with length for a $1mm$ wide, $6.25\mu m$ thick polyester flexure (rotational stiffness is given by $\kappa = \frac{EI}{l}$ where the area moment of inertia I varies as t^3).

Good adhesion between the polyester flexures and the steel links has been difficult to achieve and *peeling* of the flexure away from the steel surface during actuation was a significant problem. Cyanoacrylate adhesives bond well to steel so one solution is to employ steel plates on either side of the polyester to "sandwich" the flexure. Unfortunately, these clamps add an additional level of complexity to the template design and assembly stage so the use of MEMS to fabricate polyimide flexures, as done by Suzuki *et al* in [15], is worthwhile pursuing. Another problem with the polyester flexures is that very little compressive force is required to cause buckling. The four-bar base joint is susceptible to this problem due to high translational forces, thus the cross-flexure described by Blanding in [2] was utilized there to prevent such buckling.

3 Structural Dynamics

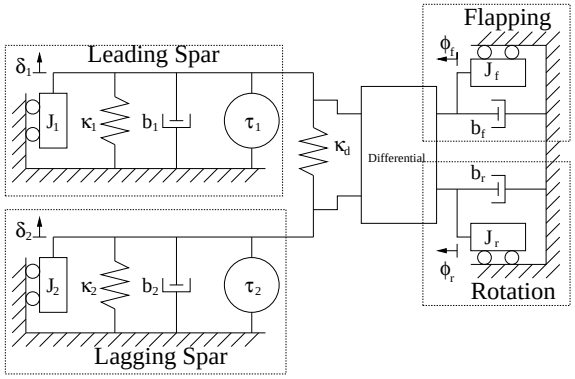

Figure 10: Translational model of 2 DOF Dynamics

Figure 10 shows a simplified dynamic model for control of the 2 DOF wing. The model is composed of rotational elements but is illustrated with the more familiar translational analogs. The leading spar is represented by the system shown in the top left corner (the transmission ratios are absorbed into the lumped model) consisting of a mass-spring-damper (J_1, κ_1, and b_1) and input torque (τ_1). The lagging spar is similarly represented by J_2, κ_2, b_2 and τ_2. The differential mechanism couples the spar motions through a differential stiffness κ_d and transforms the actuator input angular positions δ_1 and δ_2 into output flapping and rotation angles, ϕ_f and ϕ_r, respectively. Each output

motion also has associated inertia and damping terms (J_f, J_r, b_f and b_r).

This simplified model results in a fourth order system with two inputs and two outputs. For small angles, a linearized dynamic model can be generated. The differential mapping is given by

$$\begin{bmatrix} \phi_f \\ \phi_r \end{bmatrix} = T \begin{bmatrix} \frac{1}{2} & \frac{1}{2} \\ \lambda & -\lambda \end{bmatrix} \begin{bmatrix} \delta_1 \\ \delta_2 \end{bmatrix} \tag{4}$$

where T is the transmission ratio from actuator input angle to spar output angle and λ is the transmission ratio from spar phase angle to rotation angle.

For large T, inertia and damping terms in the four-bars are negligible. Assuming symmetry in the design, further simplification is achieved by setting $\kappa_1 = \kappa_2$. The equations of motion then become

$$\tau = \begin{bmatrix} J_a & J_b \\ J_b & J_a \end{bmatrix} \ddot{\delta} + \begin{bmatrix} B_a & B_b \\ B_b & B_a \end{bmatrix} \dot{\delta} + \begin{bmatrix} \kappa_1 + \kappa_d & -\kappa_d \\ -\kappa_d & \kappa_1 + \kappa_d \end{bmatrix} \delta \tag{5}$$

where

$$\begin{aligned} J_{a,b} &= T^2 \left(\frac{J_f}{4} \pm \lambda^2 J_r \right) \\ B_{a,b} &= T^2 \left(\frac{b_f}{4} \pm \lambda^2 b_r \right) \end{aligned} \tag{6}$$

This system has two resonant frequencies which have in-phase and out-of-phase natural motion modes which are associated with flapping and rotational flapping frequencies, respectively. These frequencies are given by

$$\begin{aligned} \omega_1^2 &= \frac{2\kappa_1}{T^2 J_f} \\ \omega_2^2 &= \frac{\kappa_1 + 2\kappa_d}{2\lambda^2 T^2 J_r} \end{aligned} \tag{7}$$

3.1 Actuation Experimental Results

Experiments were conducted using $16mm \times 3mm$ PZT unimorphs, fabricated using techniques described by Sitti *et al* [14], connected to the two four-bars coupled through a differential. The initial structure had widely mismatched flapping and rotational resonant frequencies. By adding a bar structure at the base with rotational inertia of approximately $10^{-10} kg \cdot m^2$, the resonances were closely matched. The design of the wing differential introduces an inherent asymmetry between the leading and lagging spar dynamics which currently is not accounted for in the model. Experimentally, the resonant frequencies of the leading and lagging spars were observed to be $38Hz$ and $32Hz$, respectively. Their amplitudes were matched at $34Hz$. It is to be noted that without proper inertia balancing, the spars are dynamically coupled, thus independent spar control is not possible.

Estimated values for parameters to be used in equation (7) (effective values with respect to actuator coordinates) are as follows: transmission ratios are $T = 50$ and $\lambda = 1.25$, rotational stiffness values are $\kappa_1 = 5.30 \times 10^{-2} N \cdot m/rad$ and $\kappa_d = 2.07 \times 10^{-2}\ Nm/rad$, damping coefficients are $b_f = 2.1 \times 10^{-8}\ N \cdot m \cdot s/rad$ and $b_r = 3.3 \times 10^{-9}\ N \cdot m \cdot s/rad$, and inertia moments are $J_f = 1.6 \times 10^{-10}\ kg \cdot m^2$ and $J_r = 1.0 \times 10^{-10}\ kg \cdot m^2$. The calculated resonant frequencies of f_1 and f_2 are computed to be 81.9 Hz and 55.3 Hz, respectively. These are significantly higher than the observed resonant frequencies, likely owing to crude approximations of the parameter values. For example, stiffness estimates are based on ideal pin joints with purely rotational springs, ignoring the translational compliance of the flexures. Furthermore, transmission ratios used are for the nominal position but these ratios are also local minima at this position so the effective ratios are higher. Both of these factors result in calculations which overestimate resonant frequencies.

Figure 11 shows some high-speed video images of typical flapping and rotational motions which were generated by tuning the phase between the $35Hz$ sinusoidal voltage inputs to the piezo unimorphs.

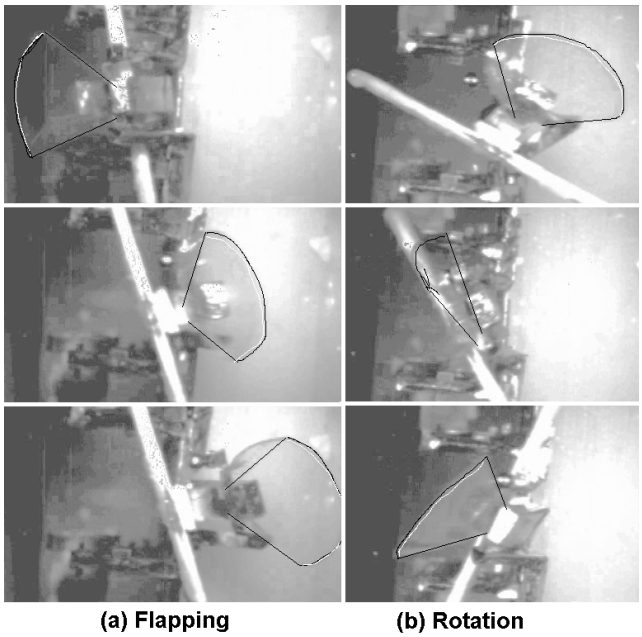

Figure 11: Typical trajectories at $35Hz$ for (a) flapping and (b) rotation (observe the motion of the white rod which rotates along with the wing).

4 Wing Force Sensing

Measurement of wing forces is achieved using semiconductor strain gauges mounted directly on the wing spars. These measurements serve the dual purpose of initial off-line characterization of forces generated during wing motion and eventually for feedback in the real-time wing control system. Measurements described in this section are from experiments with a 1.3X scale structure.

Considering the wing spar as a rigid body, the moment M is directly proportional to the strain ϵ:

$$M = \frac{EI\epsilon}{z} \tag{8}$$

where E is the wing elastic modulus, I is the cross-sectional moment of inertia and z is the distance of the gauge from the neutral axis. The force, F, is directly proportional to this moment:

$$F = \frac{M}{x - x_F} \tag{9}$$

where the force acts at a distance x_F from the base of the spar. The unit x represents the distance from the fixed end of the cantilever to the point of measurement (the center of the gauge).

Initially, a single gauge was placed on the wing spar to measure the inertial and aerodynamic forces felt on the tip of the spar. The gauge was mounted to a polystyrene spar and positioned on the four-bar (see Figure 12). The position of the gauge along the spar is crucial for the sensitivity of the measurements (see [1] and [6] for a discussion on force sensors and sensor placement). For a given force, the maximum moment, and thus the maximum strain is measured when the gauge is placed as close to the base of the cantilever as possible. This is clear from equation (9).

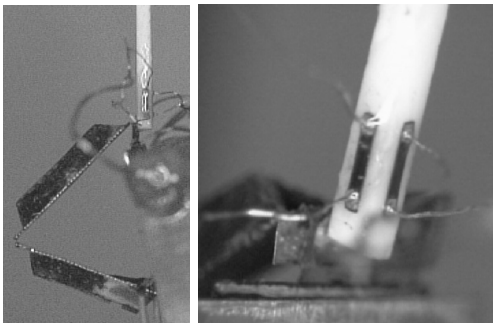

Figure 12: Photos of $1mm$ strain gauge mounted on 1.3X spar (a) attached to a four-bar and (b) close-up of wiring.

During a wing stroke, a force distribution develops along the wing spar. For a rigid body, this force distribution can be reduced to a single force acting at the center of force of the distribution. Using a pair of gauges located at two positions along the wing spar, both the equivalent force F_{eq} and the center of force x_{eq} can be solved from the system of equations:

$$M_i = F_{eq}(x_i - x_{eq}) \tag{10}$$

where M_i and x_i $(i = 1, 2)$ are the measured moment and gauge position along the spar, respectively. Using a dual-axis force sensor in which the gauges are mounted orthogonal to each other, the force can be resolved into two components orthogonal to the wing spar. The component which is also orthogonal to the stroke plane is related to the lift force while the other component is related to the drag force.

A 1.3X wing spar was constructed from a $0.5mm$ square polystyrene wing spar, $10mm$ long with semiconductor strain gauges mounted on two adjacent faces of the spar. The sensitivity of the system was measured to be less than $10\mu N$, based on $E = 3GPa$, $I = 5.2 \times 10^{-15} m^4$, $z = 250\mu m$, and a minimum readable strain from the gauges of $0.1\mu\epsilon$. This gives a usable resolution with off-the-shelf strain gauge amplifiers.

Since the wing must go through large stroke and rotation angles, the wiring to the gauges presents problems, not only with fatigue of the wires, but also with added parallel stiffness. Thus, the forces sensors are currently being designed to measure the forces at the base of the four-bar, then utilize the differential mapping to estimate the wing forces. Wiring of the gauges at the final scale is also extremely difficult. To alleviate this, a wing fabricated using MEMS technology is being pursued, with built-in strain gauges and amplification circuitry.

4.1 Sensing Experimental Results

The 1.3X scale structure was fitted with a mylar wing which could be rotated to change the attack angle. The wing was driven at $80Hz$ with a stroke amplitude of 60^o. The raw data extracted from the force sensors consists of both the spar inertial forces and the wing aerodynamic forces. This total force is not, in itself, useful but the inertial force can be determined separately, by placing an equivalent point mass with negligible area at the end of a cantilever and repeating the experiment. The aerodynamic force can then be determined as the difference between the total force and the inertial force. Figure 13 shows the resulting lift and drag forces measured on the wing after accounting for the inertial force. The calculation for the

center of force shows that the location stays roughly constant which is in agreement with the assumption made by Dickinson *et al* [4].

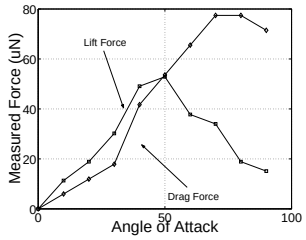

Figure 13: Measured lift and drag forces vs. attack angle for the 1.3X spar.

5 Wing Control Issues

There are some interesting control problems for the MFI. In this section, issues related only to low-level control are discussed in which tracking of a wing force or position trajectory is desired.

One problem that needs to be addressed is that the thorax will be driven near resonance, a mode which is typically purposely suppressed in most control applications. As a result, the phase lag between the input actuation signal and the motion is 90^o, effectively introducing a "time delay" into the control. Thus, there are no ways to control the position of the wing except on a stroke-by-stroke basis; there is evidence to suggest this is true even for biological flying insects. Since the forces measured by the strain gauges are mostly inertial (accounting for more than $\frac{2}{3}$ of the measurement along the drag axis), it is possible to use these signals as a feedback for a control system. This problem is compounded by the existence of distinct resonant frequencies for flapping and for rotation, as described in section 3.

A switching controller which sets the piezoelectric unimorph voltage to $\pm V_{max}$ adds complexity to the problem by making it a hybrid system. Nonlinear, time-varying terms are introduced by the piezoelectric material and the unknown aerodynamic drag.

Robustness will be an important concern and stochastic models of the noise and disturbances which may be encountered (*e.g.,* measurement noise, wind gusts, *etc.*) need to be developed.

Figure 14 shows a block diagram realization for a wing controller. The control is based upon a desired force signal, generated on a stroke-by-stroke basis (or half-stroke-by-half-stroke basis). The reference force signal, generated by the high level MFI controller, is compared to the actual force measured by the wing

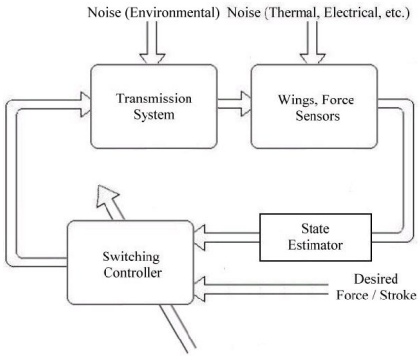

Figure 14: Wing controller

spar force sensors. The raw force measured by the wing spar sensors consists of the combination of inertial and aerodynamic forces. The force measured by the sensor, F, is modeled by the expression:

$$F = m_s\ddot{x} + b_w(x, \dot{x}, t) + k_s x \tag{11}$$

where m_s is the spar mass, k_s is the spar stiffness, and $b_w(\cdot, \cdot, t)$ is the nonlinear, time-varying wing damping. For the control experiment in this paper, this damping is taken to be LTI (*i.e.,* $b_w(x, \dot{x}, t) = b_w\dot{x}$).

5.1 Example Wing Trajectory

The wing trajectory of an insect is characterized by numerous parameters including stroke angle, rotation angle, attack angle, frequency, upstroke-to-downstroke time ratio, dorsal and ventral flip timing and deviation from the stroke plane (in the current MFI thorax design, this parameter cannot be controlled).

An example wing trajectory was generated using the following parameters: stroke of $\pm 70^o$, rotation of $\pm 45^o$, 30^o angle of attack, frequency of $f = 1/T = 150Hz$, downstroke time of $0.7T$, upstroke time of $0.3T$, and $\pm 0.1T$ start and end of the dorsal and ventral flip timing. The resulting kinematic flapping and rotation angles are shown as a function of time in Figure 15(a). Solving the inverse kinematic relations gives the necessary unimorph displacements to generate the desired trajectory (see Figure 15(b)).

For the MFI, force control is more appropriate than position control because of the need to generate lift forces. A simple sawtooth signal was selected as a force reference trajectory for the 5X model. This signal is an interesting one to track because of the asymmetry and the high frequency components. A simple PD controller was employed using this trajectory and the force signal to generate the results in Figure 16. Similar experiments will be performed on an instrumented final-sized structure once it has been fabricated.

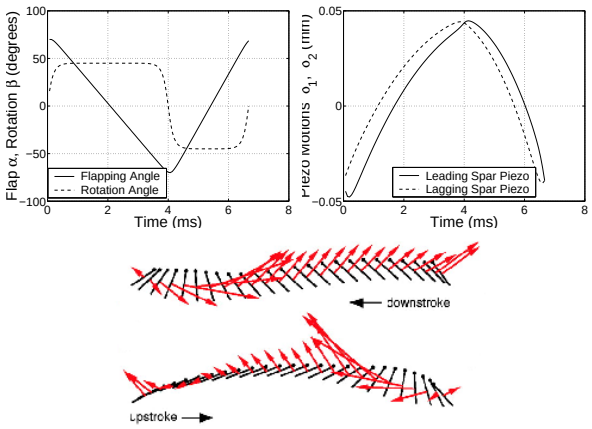

Figure 15: (a) Desired flapping and rotation motions; (b) Required unimorph displacements; (c) Wing chord positions separated by constant time intervals and instantaneous forces (modified from [4]).

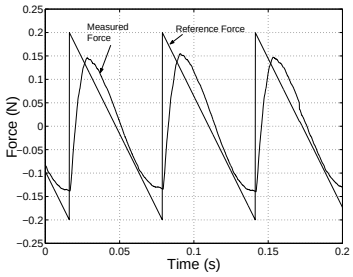

Figure 16: Force tracking experiment.

6 Discussion

This paper presents aspects of the UC Berkeley MFI project, specifically related to the actuation, sensing and control. In the near term, the thorax structure described in section 2.2 will be constructed at final size and instrumented with the strain gauges described in section 4. Various control strategies will be employed and compared for their force generation and tracking capabilities.

Acknowledgments

The authors thank M. Dickinson and S. Sane for insight into insect flight, T. Su for unimorph fabrication, J. Thompson for laser-cutting tools, and G. Moy and K.H. Chiang for discussions on structural design.

References

[1] A. Bicchi, A. Caiti, and D. Prattichizzo. Optimal design of a multi-axis force/torque sensor. In *Proc of IEEE Intl Conf on Decision and Control*, pages 2981–2986, Phoenix, AZ, Dec 1999.

[2] D.L. Blanding. Using "exact constraint" to design flexure mechanisms. In *Proc. of ASME Dyn Sys and Control Div*, volume 69-2, Orlando, FL, Nov 5-10 2000.

[3] A. Cox, E. Garcia, and M. Goldfarb. Actuator development for a flapping microrobotic mav. In *SPIE Microrobotics Symp*, pages 102–108, Boston, MA, Nov 1998.

[4] M.H. Dickinson, F-O. Lehmann, and S.P. Sane. Wing rotation and the aerodynamic basis of insect flight. *Science*, 284:1954–1960, June 1999.

[5] C.P. Ellington, C. van den Berg, A.P. Willmot, and A.L.R. Thomas. Leading edge vortices in insect flight. *Nature*, 384:626–630, December 1996.

[6] S. Fahlbusch and S. Fatikow. Force sensing in microrobotic systems - an overview. In *Proc of IEEE Intl Conf on Electronics, Circuits and Systems*, pages 259–262, Lisbon, Portugal, Sept 1998.

[7] R.S. Fearing, K.H. Chiang, M.H. Dickinson, D.L. Pick, M. Sitti, and J. Yan. Wing transmission for a micromechanical flying insect. In *Proc of IEEE Intl Conf on Robotics and Automation*, pages 1509–1516, San Francisco, CA, April 2000.

[8] R.H. Francis and J. Cohen. The flow near a wing which starts suddenly from rest and then stalls. *Rep Memo Aeronaut Res Comm*, 1561, 1933.

[9] Y. Kubo, I. Shimoyama, T. Kaneda, and H. Miura. Study on wings of flying microrobots. In *Proc of IEEE Intl Conf on Robotics and Automation*, pages 834–839, San Diego, CA, May 1994.

[10] B. Motazed, D. Vos, and M. Drela. Aerodynamics and flight control design for hovering MAVs. In *Proc of Amer Control Conf*, Philadelphia, PA, June 1998.

[11] T.N. Pornsin-Sirirak, S.W. Lee, H. Nassef, J. Grasmeyer, Y.C. Tai, C.M. Ho, and M. Keennon. MEMS wing technology for a battery-powered ornithopter. In *Proc. of IEEE 13th Annual Intl Conf on MEMS*, pages 799–804, Piscataway, NJ, Jan 2000.

[12] E. Shimada, J.A. Thompson, J. Yan, R.J. Wood, and R.S. Fearing. Prototyping millirobots using dextrous microassembly and folding. In *Symp on Microrobotics ASME Intl Mech Eng Cong and Expo*, Orlando, FL, Nov 5-10 2000.

[13] I. Shimoyama, H. Miura, K. Suzuki, and Y. Ezura. Insect-like microrobots with external skeletons. *IEEE Control Systems Magazine*, 13:37–41, February 1993.

[14] M. Sitti, T. Su, R.S. Fearing, D. Campolo, J. Yan, D. Taylor, and T. Sands. Development of PZT and PZN-PT based unimorph actuators for micromechanical flapping mechanism. In *Proc of IEEE Intl Conf on Robotics and Automation*, Seoul, Korea, May 2001.

[15] K. Suzuki, I. Shimoyama, and H. Miura. Insect-model based microrobot with elastic hinges. *IEEE MEMS*, 3:4–9, March 1994.